
GS-OCTREE: OCTREE-BASED 3D GAUSSIAN SPLATTING FOR ROBUST OBJECT-LEVEL 3D RECONSTRUCTION UNDER STRONG LIGHTING

A PREPRINT

Jiaze Li*

College of Computing and Data Science
Nanyang Technological University
Singapore

Zhengyu Wen*

College of Computing and Data Science
Nanyang Technological University
Singapore

Luo Zhang*

College of Computing and Data Science
Nanyang Technological University
Singapore

Jiangbei Hu

International School of Information Science & Engineering
Dalian University of Technology
China

Fei Hou

Institute of Software
Chinese Academy of Sciences
China

Zhebin Zhang

InnoPeak Technology, Inc.
United States of America

Ying He[†]

College of Computing and Data Science
Nanyang Technological University
Singapore

June 27, 2024

ABSTRACT

The 3D Gaussian Splatting technique has significantly advanced the construction of radiance fields from multi-view images, enabling real-time rendering. While point-based rasterization effectively reduces computational demands for rendering, it often struggles to accurately reconstruct the geometry of the target object, especially under strong lighting. To address this challenge, we introduce a novel approach that combines octree-based implicit surface representations with Gaussian splatting. Our method consists of four stages. Initially, it reconstructs a signed distance field (SDF) and a radiance field through volume rendering, encoding them in a low-resolution octree. The initial SDF represents the coarse geometry of the target object. Subsequently, it introduces 3D Gaussians as additional degrees of freedom, which are guided by the SDF. In the third stage, the optimized Gaussians further improve the accuracy of the SDF, allowing it to recover finer geometric details compared to the initial SDF obtained in the first stage. Finally, it adopts the refined SDF to further optimize the 3D Gaussians via splatting, eliminating those that contribute little to visual appearance. Experimental results show that our method, which leverages the distribution of 3D Gaussians with SDFs, reconstructs more accurate geometry, particularly in images with specular highlights caused by strong lighting.

1 Introduction

Reconstructing 3D geometry and appearance from multi-view images is a critical area in 3D vision. Recently, Neural Radiance Field (NeRF) based methods Mildenhall et al. [2021], Barron et al. [2021, 2022] have significantly advanced the state-of-the-art for this problem. However, these methods often face challenges with long training times and slow rendering speeds due to the complexity of optimizing neural networks. To enhance training speed and reduce rendering

*J. Li, Z. Wen and L. Zhang contribute equally to the project.

[†]Corresponding author: Y. He (yhe@ntu.edu.sg)

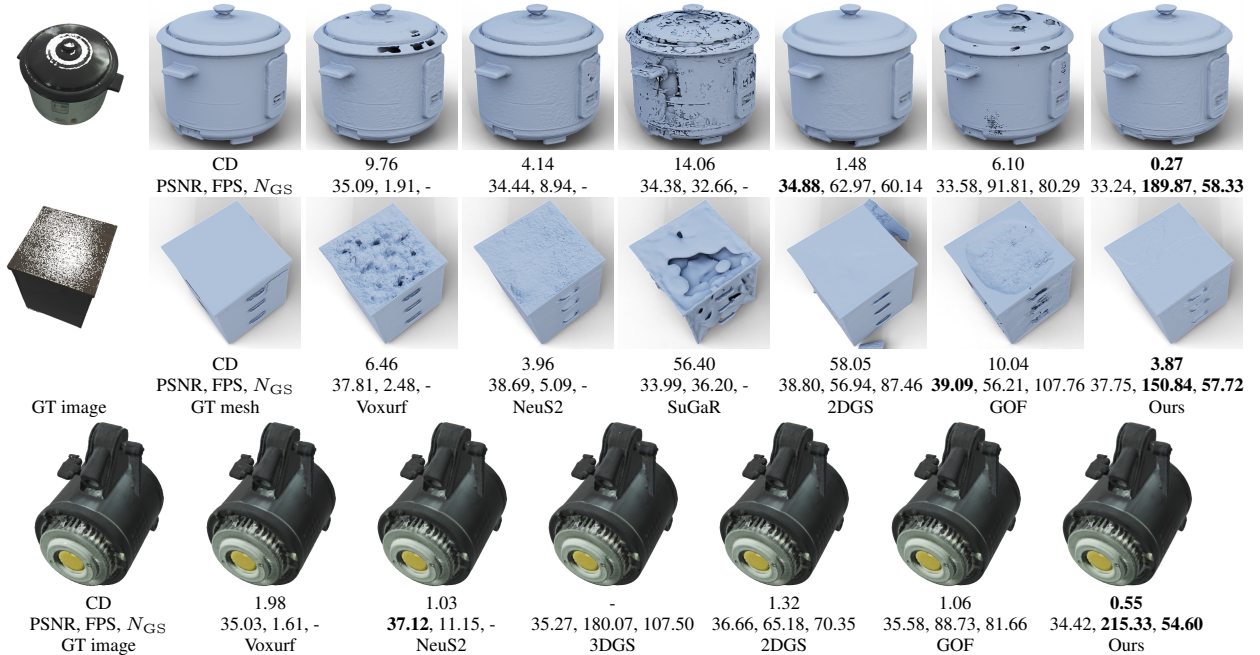


Figure 1: Our method integrates octree-based implicit surface representations with Gaussian splatting, enabling real-time rendering for novel view synthesis using fewer Gaussians. This integration allows us to robustly reconstruct high-quality geometry from input images with large areas of specular highlight due to strong lighting. The values below each figure represent the Chamfer distance (10^{-4}), PSNR, FPS and the number of Gaussians N_{GS} (in thousands), with the best results highlighted in bold.

time while maintaining quality, some methods adopt explicit representations to store features Fridovich-Keil et al. [2022], Wu et al. [2023a], Sun et al. [2022a], Liu et al. [2020]. While these approaches offer faster rendering compared to implicit methods, they often struggle with accurate geometric reconstruction. Furthermore, the lack of compactness in these methods poses challenges in improving resolution and reconstruction accuracy. These limitations are primarily due to the constraints of density-based volume rendering, which relies on the precision of the grid and the initial structure setup. To address these issues, DVGO Sun et al. [2022a] and DVGOv2 Sun et al. [2022b] integrate explicit and implicit methods by employing a shallow multi-layer perception (MLP) on the voxel grid representing features, achieving a better balance between the quality and efficiency of novel view synthesis.

Recently, 3D Gaussian Splatting (3DGS) Kerbl et al. [2023] has emerged as a promising direction for differentiable rendering. It enables efficient training and rendering by optimizing many 3D Gaussian points, yielding visually appealing results. However, due to the lack of geometric constraints, 3DGS struggles to reconstruct high-quality geometry. Subsequent works, such as Guédon and Lepetit [2024], Chen et al. [2023], Tang et al. [2024], Yi et al. [2024], Yu et al. [2024], Huang et al. [2024], attempt to extract explicit geometries from Gaussian splatting. For instance, 2DGS Huang et al. [2024] deforms 3D Gaussians into 2D oriented disks and utilises them to model surfaces, significantly improving scene-level geometry quality. However, for object-level reconstruction, particularly when the target object contains regions with relatively few views in the input images, 2DGS often yields suboptimal results with redundant components. Consequently, the geometry quality is not comparable to pure volume-rendering-based neural methods, such as Voxurf Wu et al. [2023a] and NeuS2 Wang et al. [2023a]. GOF Yu et al. [2024] induces a Gaussian opacity field from 3D Gaussians and extracts its level set through efficient marching tetrahedra, further improving the quality of geometry extracted from 3DGS Kerbl et al. [2023]. However, its surface extraction, which relies on opacity, is sensitive to strong lighting. In regions with strong light, the opacity is often very low, resulting in holes in the reconstructed surface at those positions.

Volume rendering-based methods, such as VolSDF Yariv et al. [2021], NeuS Wang et al. [2021], NeuS2 Wang et al. [2023a] and Voxurf Wu et al. [2023a], can achieve high geometric quality in object level reconstruction, however, strong lighting makes the color of object surface change dramatically under different view directions which can disrupt the reconstruction of its opacity field, resulting in inaccurate geometry surface reconstruction. We found that the position of 3DGS points is robust to strong light, as Gaussian points can still surround the surface of the object even under strong light, which can assist the volume rendering framework to generate more accurate geometry under strong light. In this

paper, we propose a novel octree-based method for reconstructing object-level implicit surfaces under strong light. We formulate the reconstruction as a coarse-to-fine optimization problem, guided by SDF and 3D Gaussians, without relying on any neural networks. Our method consists of four stages. Initially, it reconstructs an SDF and a radiance field through volume rendering, encoding the coarse geometry of the target object in an octree with low resolution. Subsequently, it introduces 3D Gaussians as additional degrees of freedom, optimized through the progressive refinement of the octree, guided by the SDF. In the third stage, the optimized Gaussians further improve the accuracy of the SDF, enabling the recovery of finer geometric details by pulling surfaces towards 3D Gaussian points, offsetting the artefacts caused by specular highlights. Finally, the refined SDF is utilised to further optimize 3D Gaussians via splatting, eliminating those that contribute little to the visual appearance. See Fig 1 for a comparative illustration of the results generated by ours and other methods.

We summarize our main contributions as follows:

- We introduce a novel octree-based representation that seamlessly combines SDFs and 3D Gaussians, enabling real-time rendering with high-quality geometric surface reconstruction.
- Our approach harnesses the complementary advantages of SDF and 3D Gaussian representations, enabling the reconstruction of accurate geometry even in the presence of strong lighting. Our methods also reduce the number of 3D Gaussians by more than 50% while preserving competitive rendering quality and fast rendering speed.
- Our octree-based method allows for more efficient computation of high-order derivatives of the information field. This enables us to introduce singular-Hessian loss to enhance the reconstruction of geometry.

2 Related Work

2.1 Neural Implicit Surfaces

NeRF Mildenhall et al. [2021] utilizes neural volume rendering to synthesize pixel colors from multiple points sampled on each camera ray. However, it lacks a practical constraint on the reconstructed geometry’s surface, relying on threshold settings in its volume density function, which can introduce noise and potential issues with the reconstructed geometry. In contrast, methods based on neural implicit surface functions (e.g., occupancy fields and SDFs) achieve superior surface modeling and geometric reconstruction without compromising the quality of visual appearance Yariv et al. [2020], Niemeyer et al. [2020]. However, these approaches often require 2D mask supervision for training, which can be challenging. NeuS Wang et al. [2021], VolSDF Yariv et al. [2021] and their many follow-up works naturally combine neural volume rendering with SDFs and are able to achieve high-quality geometry for object-level reconstruction. However, it is hard to extend these methods to scene-level reconstruction tasks.

2.2 Training Performance Improvement

Training neural radiance fields and their implicit surface-based variants, such as NeuS Wang et al. [2021] and VolSDF Yariv et al. [2021], require significant computational resources. Various techniques Müller et al. [2022], Rosu and Behnke [2023] have been proposed to reduce the training cost. For example, INGP Müller et al. [2022] achieves a substantial reduction in the number of training parameters through the implementation of multi-resolution hash coding coupled with highly optimized CUDA kernels. NeuS2 Wang et al. [2023a], PermutoSDF Rosu and Behnke [2023], and Neuralangelo Li et al. [2023] employ multi-resolution hash encodings and shallow MLPs proposed in INGP to replace a large neural network for accelerating NeuS training. DVGO Sun et al. [2022a] and Voxurf Wu et al. [2023a] achieve training acceleration by incorporating both voxelization and smaller MLPs. PermutoSDF Rosu and Behnke [2023] employed a triangular pyramid grid for reducing calculation overhead during interpolation. TensorRF Chen et al. [2022] and Strivec Gao et al. [2023] leverage tensor decomposition for tensor grid modeling. However, most methods are limited by the network structure and cannot achieve high-speed rendering.

2.3 Real-time Rendering

Various strategies Garbin et al. [2021], Yu et al. [2021], Wang et al. [2022] have been proposed for significantly increasing rendering speeds. For example, Plenocree Yu et al. [2021] and RT-Octree Shu et al. [2023] expedite the process by converting NeRF models into an explicit octree, while Plenoxels Fridovich-Keil et al. [2022] adopts voxel-based representation for fast rendering. Additionally, BakedSDF Yariv et al. [2023] pre-calculates and stores rendering parameters through the baking method, enabling a smaller MLP to swiftly read these parameters during rendering.

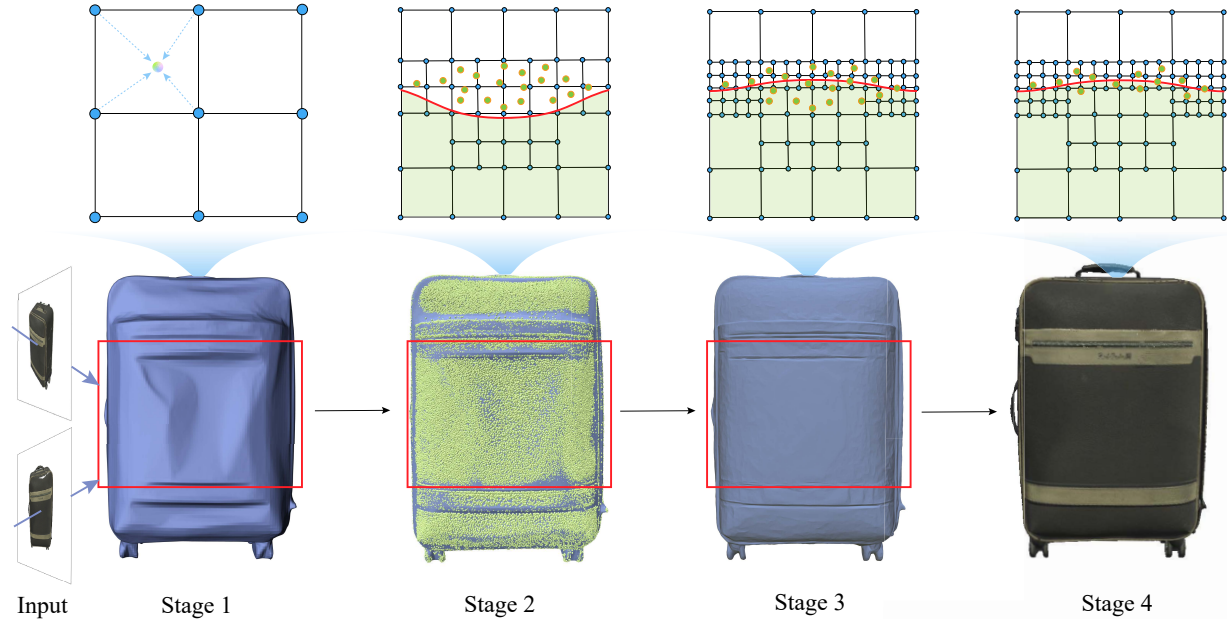


Figure 2: **Algorithmic pipeline.** Our framework consists mainly of four stages. Utilizing the octree, we progressively optimize the signed distance values s_{ij} for geometry and the SH coefficients \mathbf{a}_{ij} for radiance for each octree node in a coarse-to-fine manner, alternating between volume rendering and point splatting.

2.4 3D Gaussian Splatting

The recently proposed 3D Gaussian Splatting Kerbl et al. [2023] takes a completely different approach from volume rendering-based neural radiance fields. It innovatively integrates point-based rendering and differentiable rendering, achieving real-time rendering through efficient parallel computing. Moreover, the explicit modelling of 3D scenes with Gaussians provides a shortcut for controlling the dynamics of a scene, particularly crucial in complex situations with diverse geometries and changing lighting conditions.

The capability for control and modification, coupled with an efficient rendering process, positions 3DGS as a revolutionary technique in shaping multi-view 3D reconstruction Guédon and Lepetit [2024], Chen et al. [2023], Lu et al. [2024], Xiong et al. [2024], Lyu et al. [2024], Yu et al. [2024], Huang et al. [2024]. SuGaR Guédon and Lepetit [2024] optimizes the position of 3D Gaussians by aligning them with the surfaces and using an SDF to guide the position and orientation of 3D Gaussians. Meanwhile, NeuSG Chen et al. [2023] leverages NeuS Wang et al. [2021] with 3D Gaussian guidance to enhance the optimization process of NeuS-generated SDF. GOF Yu et al. [2024] establishes a Gaussian opacity field from 3D Gaussians and provides an approximation of surface normals. 2DGS Huang et al. [2024] models the surfaces by using flat 3D Gaussians, deforming them into 2D oriented Gaussian disks. 3DGSR Lyu et al. [2024] trains an SDF and proposes a differentiable SDF-to-opacity transformation function, to generate corresponding opacities of 3D Gaussians.

Although 3DGS is capable of reconstructing scene-level geometries, current 3DGS-based reconstruction methods Yu et al. [2024], Huang et al. [2024] are not robust to specular highlights in images or need postprocessing to remove floating surfaces. Our method addresses these challenges by jointly optimizing 3DGS with octree-encoded SDFs. Leveraging the network-free feature of our method, we can utilize effective geometric regularizers with high-order derivatives, such as the singular Hessian loss, to improve the quality of the geometry. We refer readers to recent surveys Fei et al. [2024], Wu et al. [2024], Chen and Wang [2024] for a comprehensive overview of 3DGS techniques.

3 Preliminaries

3.1 Volume Rendering

The volume rendering technique Mildenhall et al. [2021] synthesizes pixel colors for the output images by utilizing 3D fields of radiances \mathbf{c} and densities σ . Specifically, color is computed by integrating along ray \mathbf{r} shooting from the

camera position \mathbf{o} with sampling points $\{\mathbf{o} + t_i \mathbf{d}\}_{i=1}^N$ as

$$\mathbf{C}(\mathbf{r}) = \sum_i^N T_i (1 - \exp(-\sigma_i \delta_i)) \mathbf{c}_i, \quad (1)$$

where $T_i = \exp(-\sum_{j=1}^{i-1} \sigma_j \delta_j)$ represents the transparency, and δ_i is the distance between sampling points. NeRF Mildenhall et al. [2021] employs a neural network to learn radiance fields from the given multi-view images. However, its inefficiency in training and inference has spurred the recent development of network-free methods, such as 3DGS Kerbl et al. [2023].

Neural implicit surface-based methods, such as NeuS Wang et al. [2021] and VolSDF Yariv et al. [2021], jointly learn an SDF \mathcal{S} and a radiance field \mathbf{c} from the input images. To enable volume rendering, they convert the SDF $\mathcal{S}(\mathbf{x})$ into volume density as follows:

$$\sigma(\mathbf{x}) = \begin{cases} \frac{1}{2\beta} \exp(\frac{\mathcal{S}(\mathbf{x})}{\beta}) & \text{if } \mathcal{S}(\mathbf{x}) \leq 0, \\ \frac{1}{\beta} - \frac{1}{2\beta} \exp(-\frac{\mathcal{S}(\mathbf{x})}{\beta}) & \text{if } \mathcal{S}(\mathbf{x}) > 0, \end{cases} \quad (2)$$

where β is a learnable parameter to adjust the smoothness of the density function σ near the object boundary. In our framework, we introduce an octree-based structure to encode both SDFs and radiances, enabling real-time volume rendering.

3.2 Point-Based Rendering

3DGS Kerbl et al. [2023] utilizes an ensemble of 3D Gaussians to represent the radiance fields, offering greater flexibility and efficiency than volumetric radiance fields. Specifically, a Gaussian at position \mathbf{x} is defined as

$$G(\mathbf{x}) = e^{-\frac{1}{2} \mathbf{x}^T \Sigma^{-1} \mathbf{x}}, \quad (3)$$

where Σ is the covariance matrix controlling the size and orientation of the Gaussian. During rendering, the 3D Gaussians $G(\mathbf{x})$ are first transformed into 2D Gaussians $G'(\mathbf{x})$ on the projected image plane. After that, a tile-based rasterizer is applied to split the image plane into tiles and sort these 2D Gaussians efficiently. Finally, α -blending is performed on these 2D Gaussians and the color of each pixel is obtained as follows:

$$C(\mathbf{x}') = \sum_{i \in N} c_i \sigma_i \prod_{j=1}^{i-1} (1 - \sigma_j), \sigma_i = \alpha_i G'_i(\mathbf{x}'), \quad (4)$$

where \mathbf{x}' is the pixel positions on the image plane and α_i is the opacity of the i -th Gaussian. The parameters of Gaussian functions can be directly optimized using a gradient-based solver without neural networks, significantly improving the training and rendering efficiency.

4 Method

Overview. As illustrated in Figure 2, our method consists of four stages. In Stage 1, we learn an implicit surface under volume rendering and encode it by a low-resolution octree, representing the rough geometry of the target object. In Stage 2, we initialize a point cloud G_p from the SDF obtained in Stage 1 and optimize the position of each point under point splatting. In Stage 3, we leverage the optimized G_p to improve the geometry of the SDF via progressively refining the octree. At the end of this stage, we obtain an implicit surface with high-quality geometry. Finally, in Stage 4, we further optimize the number and positions of Gaussians under the guidance of SDF, eliminating the points that contribute little to the rendering. The final images are then produced in real-time by applying point splatting to the finalized 3D Gaussians.

4.1 Octree-based 3D Reconstruction

As a hierarchical data structure, octree is well-suited for managing complex spatial information [Wilhelms and Van Gelder 1992]. It starts with a root node representing a cubical region, which iteratively subdivides into octants according to the data contained in each node. We define the final subdivided grid as leaf nodes $\ell_i, i \in I^l$, where l is the subdivision level of this node, and I^l is the total number of nodes at level l . Each leaf node comprises eight grid points $\{\mathbf{p}_{ij}\}_{j=1}^8$.

We store the SDF values $s_{ij} = \mathcal{S}(\mathbf{p}_{ij})$ at the octree grid points \mathbf{p}_{ij} to implicitly represent geometric shapes. We also store the SH coefficients $\mathbf{a}_{ij} = \{a_i^m\}_{ij}$ for radiance. Under the supervision of the input images, we optimize the

parameters $\Theta = \{\theta_{ij} = (s_{ij}, \mathbf{a}_{ij})\}_{i,j}$ using the gradient descent method. We use Tri-linear interpolation to compute property values for randomly selected 256 points within octree leaf nodes. We then calculate the minimum SDF value s_i for each leaf nodes, guiding further octree subdivision (see Fig. 3). With the SDFs encoded in octree, we can directly extract the zero-level set by applying the Marching Cubes algorithm to each octree node Lorensen and Cline [1998]. For reconstructing the radiance field, we convert the SDF values into density using Eq.(2) and then obtain color information for different viewpoints through SH interpolation. Subsequently, we use volume rendering to synthesize images from novel views.

Many network-based methods learn an SDF by regularizing it using the Eikonal loss \mathcal{L}_{eik} :

$$\mathcal{L}_{\text{eik}} = \int (\|\nabla \mathcal{S}(\mathbf{x})\| - 1)^2 dx \quad (5)$$

This strategy works well for SDFs encoded by a neural network. However, as pointed out by Pumarola et al. Pumarola et al. [2022], when optimizing SDFs via an explicit data structure, such as octrees, the Eikonal loss often leads to the distance value \mathcal{S} falling into undesirable minima due to the lack of the inductive bias from a neural network. To address this problem, we adopt the singular-Hessian loss proposed by Wang et al. Wang et al. [2023b], which can not only prevent the optimization from getting into unexpected local minima but also simultaneously smooth the surface, reducing noise during the optimization. Unlike traditional general-purpose smoothing items such as the Laplacian, the singular-Hessian loss, which is tailored to distance fields, has the ability to preserve geometric details to some extent while smoothing the surface. The singular-Hessian loss is defined as follows:

$$\mathcal{L}_{\text{hess}} = \frac{1}{N_s} \sum_{\tilde{p}_s^i \in P_s} \|\text{Det}(\mathbf{H}_S(\tilde{p}_s^i))\|_1 \quad \text{for } i = 1, 2, \dots, N_s, \quad (6)$$

$$\mathbf{H}_S(p) = \begin{bmatrix} D_{xx}(p) & D_{xy}(p) & D_{xz}(p) \\ D_{yx}(p) & D_{yy}(p) & D_{yz}(p) \\ D_{zx}(p) & D_{zy}(p) & D_{zz}(p) \end{bmatrix},$$

where P_s is the set of randomly sampled points around the zero level-set in the leaf nodes with max depth l_c and $l_c - 1$, and N_s is the number of samples.

Given that the octree structure is explicit, computing second-order derivatives is straightforward. Similar to Li et al. [2023], we utilize the finite difference method for this calculation. As shown in Fig. 5, for a sampled point \tilde{p}_h , we sample two additional points along each coordinate axis surrounding \tilde{p}_h with a step size of ϵ . Taking the second-order derivative on x -axis as an example, it is computed as follows:

$$D_{xx}(\tilde{p}_h) = \frac{\mathcal{S}(\tilde{p}_{h0}^x) - 2\mathcal{S}(\tilde{p}_h) + \mathcal{S}(\tilde{p}_{h1}^x)}{\epsilon^2}, \quad (7)$$

In addition, we employ the relaxing Eikonal term $\mathcal{L}_{\text{re-eik}}$ proposed by Wang et al. Wang et al. [2023b] instead of the regular Eikonal \mathcal{L}_{eik} , which allows other loss terms to play a more significant role and provides \mathcal{S} with sufficient



Figure 3: Qualitative results from octrees spanning level 6 to 9. As the resolution of the octree increases, it provides more degrees of freedom, effectively improving the quality of the reconstructed geometry.

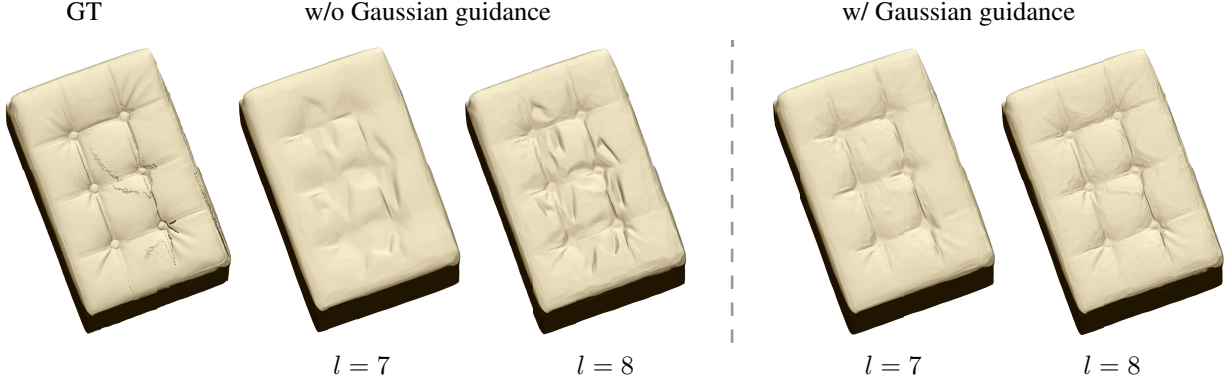


Figure 4: Gaussian-guided geometric optimization. Left: Pure octree-based SDFs are prone to inaccurate geometry, and simply refining the octree does not address the issue. Right: We propose to leverage a Gaussian point cloud generated from GS to enhance reconstruction accuracy.

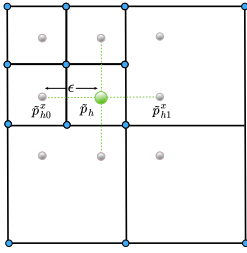


Figure 5: We calculate the Hessian matrix using a numerical method based on octree grids.

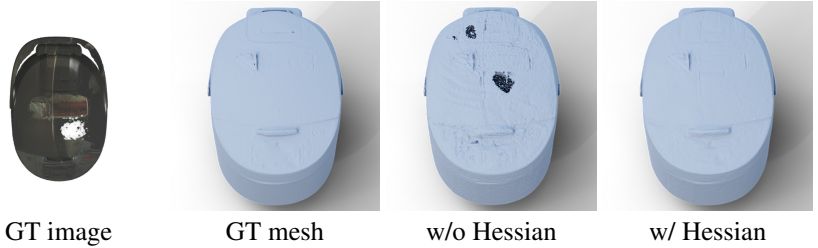


Figure 6: By incorporating the singular-Hessian loss term, we significantly reduce the artifacts generated from G_p , most of which are not on the surface and exhibit noise.

expressiveness:

$$\mathcal{L}_{\text{re-eik}} = \frac{1}{N_s} \sum_{\tilde{p}_s^i \in P_s} \text{ReLU}(\sigma_{\min} - \|\nabla S(\tilde{p}_s^i)\|) + \text{ReLU}(\|\nabla S(\tilde{p}_s^i)\| - \sigma_{\max}), \quad (8)$$

where ReLU is the operator of $\max(0, \cdot)$, and the thresholds σ_{\min} and σ_{\max} are set to 0.8 and 1.2, respectively.

4.2 Gaussian-guided Geometric Optimization

Within the volume rendering framework, eliminating artifacts such as holes, gaps, and depressions obtained from a coarse octree is not straightforward. Simply subdividing the octree, as illustrated in Fig. 4 (left), may not effectively address these issues. We observe that the Gaussians G_p progressively encircle the object surfaces throughout the GS optimization process. Motivated by this observation, we propose utilizing the point cloud G_p generated from GS to improve geometry reconstruction. Upon obtaining the SDF represented by the coarse octree following stage 1, we employ the Marching Cube method Lorensen and Cline [1998] to extract the zero isosurface, thereby generating a rough mesh M_o . We then use the positions of vertices on M_o to initialize that of G_p and optimized G_p in 3DGS pipeline for 7k iterations.

GS Loss. Although the optimized Gaussian centroids G_p mostly surround the object’s surface, few of them distribute on the surface. Thus, we cannot reconstruct the implicit surface directly from G_p . We define the following GS-points loss to make the reconstructed implicit surface just enclose the Gaussian centroids G_p ,

$$\mathcal{L}_{\text{gs}} = \frac{1}{N_g} \sum_{i=1}^{N_g} \text{ReLU}(S(\mathbf{p}_g^i) - \sigma_g), \quad \mathbf{p}_g^i \in G_p, \quad (9)$$

where N_g is the total number of Gaussian centroids, σ_g is a relaxation term since there exists noise in G_p , we set $\sigma_g = -0.01$ in our experiments. In addition, the inclusion of the singular-Hessian term as Eq.(6) can also facilitate the reduction of undesired surface variations in the geometry optimized from G_p , even though the majority of points in G_p are not on the surface and exhibit noise, as depicted in Fig. 6.

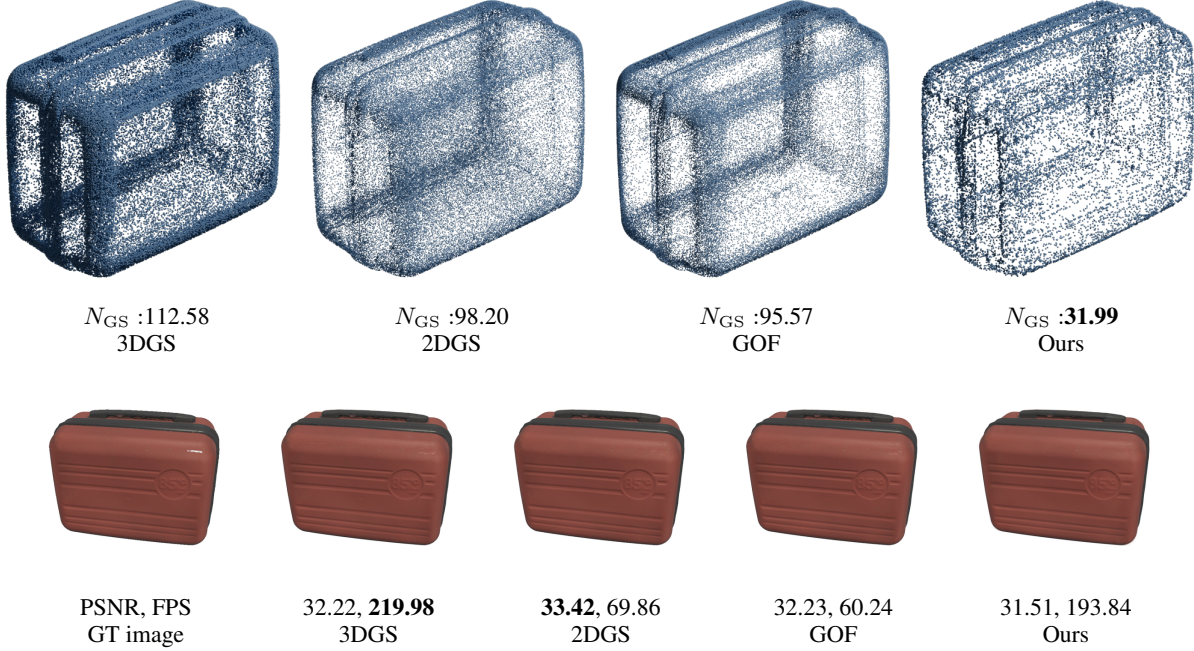


Figure 7: The visualization of 3DGS point clouds and the rendering results. The SDF successfully guides 3D Gaussians to concentrate near the object’s surface and represent the object with fewer Gaussians. It also helps to resolve the Gaussian “floaters” which bring artefacts in rendering.

Optimization. Given the discrete and sparse nature of the octree grid, we introduce a Laplacian loss term on SDF and a Total Variation loss on SH coefficients during the initialization stage. Consequently, the loss $\mathcal{L}_{\text{init}}$ in Stage 1 (Fig. 2) can be summarized as:

$$\begin{aligned}
 \mathcal{L}_{\text{init}} &= \mathcal{L}_{\text{col}} + \lambda_h \mathcal{L}_{\text{hess}} + \lambda_e \mathcal{L}_{\text{re-eik}} + \lambda_l \mathcal{L}_{\text{lap}} + \lambda_t \mathcal{L}_{\text{tv}}, \\
 \mathcal{L}_{\text{col}} &= \frac{1}{N} \sum_{n=1}^N \left\| \mathbf{C}_n - \hat{\mathbf{C}}_n \right\|_2^2, \\
 \mathcal{L}_{\text{lap}} &= \frac{1}{N_s} \sum_{\tilde{\mathbf{p}}_s^i \in P_s} \left\| D_{xx}^i + D_{yy}^i + D_{zz}^i \right\|_2^2, \\
 \mathcal{L}_{\text{tv}} &= \frac{1}{|\mathcal{V}|} \sum_{\mathbf{p} \in \mathcal{V}} \sqrt{(D_{\mathbf{p}}^x)^2 + (D_{\mathbf{p}}^y)^2 + (D_{\mathbf{p}}^z)^2},
 \end{aligned} \tag{10}$$

where N is the number of pixels. \mathcal{V} is the set of grid points. λ_h and λ_l are set to 10^{-9} and 10^{-10} , respectively. λ_e is set to 10^{-6} . λ_t is set in the range of $(10^{-5}, 10^{-3}]$, the brighter the scene, the larger λ_t is recommended. During the initialization phase, we optimize the parameters Θ and increase the octree depth from $l = 6$ to $l = 7$. Entering Stage 2, we use the vertices of M_o as the initial Gaussian centroids G_p and optimize it in 3DGS pipeline, as shown in Fig. 2. In Stage 3, we leverage the optimized G_p to facilitate further optimization of the geometry. We conduct the Stage 3 with the loss $\mathcal{L}_{\text{reco}}$ as:

$$\mathcal{L}_{\text{reco}} = \mathcal{L}_{\text{col}} + \lambda_h \mathcal{L}_{\text{hess}} + \lambda_e \mathcal{L}_{\text{re-eik}} + \lambda_g \mathcal{L}_{\text{gs}} + \lambda_t \mathcal{L}_{\text{tv}}, \tag{11}$$

where λ_h is reduced from 10^{-9} to 10^{-13} and λ_g decreases from 10^{-1} to 10^{-3} with the optimization step. TV term will be turned off after $l > 8$.

4.3 SDF-guided 3D GS Optimization

After we have got a fine-grained SDF from octree, we can utilize it to guide the optimization of 3D Gaussians further. From the observations in SuGaR Guédon and Lepetit [2024] and NeuSG Chen et al. [2023], the position of 3D Gaussians should be close to the surface of objects. Moreover, the shape of these 3D Gaussians should have a thin-plate shape, representing the colour of the nearby surface. Therefore, we applied special regularization terms to utilize the observations.

Opacity Loss. VolSDF Yariv et al. [2021] adopts an S-shaped density function to establish a correlation between opacity and signed distances for positions in space. For points near the surface, the density value should be around 0.5. For points outside the object and away from it, the opacity should be close to 0. For points buried deep inside the object, the opacity should be 1. This perspective also applies to the distribution of 3D Gaussians. Intuitively, the 3D Gaussians far away from the surface should be transparent, while the ones closer to the surface should be opaque. Moreover, there should be only a few Gaussians buried deeply inside the object since these interior Gaussians do not contribute as much as those near the surface. Therefore, we propose the following function to estimate opacity from a given signed distance value:

$$\alpha_{\text{SDF}} = \begin{cases} \frac{4e^{-k\mathcal{S}(\mathbf{p}_i)}}{(1+e^{-k\mathcal{S}(\mathbf{p}_i)})^2} & \text{if } |\mathcal{S}(\mathbf{p}_i)| < \eta, \\ 0 & \text{if } |\mathcal{S}(\mathbf{p}_i)| \geq \eta, \end{cases} \quad (12)$$

where $\mathcal{S}(\mathbf{p}_i)$ is the SDF value at position \mathbf{p}_i , and k is a scaling factor, η is the threshold value of SDF. Such an estimated opacity has a value range of $[0, 1]$, and takes 1 when the 3D Gaussians are on the surface. We truncated the estimated opacity values to 0 when Gaussian positions were too far away from the surface, and we set the threshold $\eta = 0.05$ in our experiments. According to this estimation, we proposed the following opacity loss term to guide the optimization of 3D Gaussians:

$$\mathcal{L}_{\text{op}} = \|\alpha - \alpha_{\text{SDF}}\|_2. \quad (13)$$

Scale Loss. In 3D Gaussian representations, the shape of 3D Gaussian is defined by the position $\mathbf{p} \in \mathbb{R}^3$, rotation quaternion $\mathbf{Q} \in \mathbb{R}^4$ and the scaling factors $\mathbf{S} \in \mathbb{R}^3$. In 3DGS Kerbl et al. [2023], many 3D Gaussians are located within the object surface, thus contributing little to the rendering. Therefore, to encourage the 3D Gaussians to have a thin-plate shape and close to the surface, we apply the following regularization terms proposed by Chen et al. [2023]:

$$\mathcal{L}_{\text{scale}} = \|\min(s_1, s_2, s_3)\|, \quad (14)$$

where $\mathbf{S} = \{s_1, s_2, s_3\}$ indicate the 3-dimensional scale factors. We try to minimize the smallest scale factor by Eq. (14), thus forcing the shape of the 3D Gaussians to be more flat. With the supervision of these 2 additional losses, we reduce the number of 3D Gaussians needed to represent an object, while preserving the quality of rendered images, as shown in Fig. (7). In this final stage (see Stage 4 in Fig. (2)), the loss function we use is the following:

$$\begin{aligned} \mathcal{L}_{\text{SDF-GS}} = & \mathcal{L}_1 + (1 - \lambda_{\text{ssim}})\mathcal{L}_{\text{D-SSIM}} + \lambda_{\text{op}}\mathcal{L}_{\text{op}} \\ & + \lambda_{\text{scale}}\mathcal{L}_{\text{scale}}. \end{aligned} \quad (15)$$

Here we set the default parameters $\lambda_{\text{ssim}} = 0.1$, $\lambda_{\text{op}} = 3$, and $\lambda_{\text{scale}} = 0.1$.

Table 1: Quantitative evaluation on the OO3D-SL dataset.

		Light	Ricecook	Sofa	Suitcase	Table	Toy	Avg
PSNR (\uparrow)	Voxurf	34.95	35.59	37.43	34.85	37.38	36.72	36.15
	NeuS2	35.44	35.83	36.36	35.71	38.26	36.57	36.36
	3DGS	35.70	35.09	36.50	34.87	38.63	36.87	36.28
	SuGaR	35.05	33.12	35.07	35.44	33.86	32.91	34.24
	GOF	35.55	35.31	36.49	34.81	38.66	36.85	36.28
	2DGS	36.28	36.09	35.58	35.90	39.38	37.58	36.80
	Ours	34.39	34.02	35.23	33.79	37.58	36.18	35.18
CD (\downarrow)	Voxurf	1.36	15.15	1.64	0.60	2.00	0.94	3.62
	NeuS2	1.24	1.83	2.42	0.76	1.37	1.70	1.55
	SuGaR	13.61	26.58	13.45	16.04	21.34	1.55	15.43
	GOF	1.28	7.19	2.65	1.14	4.93	1.24	3.07
	2DGS	3.89	1.56	2.96	3.86	17.16	1.68	5.18
	Ours	0.97	0.55	0.18	0.86	1.58	1.30	0.91
	FPS (\uparrow)	Voxurf	2.16	2.06	2.05	2.08	2.29	1.68
NeuS2		9.19	8.60	9.79	8.42	6.37	13.00	9.23
3DGS		142.83	217.97	200.13	183.90	165.14	328.51	206.41
SuGaR		31.79	31.71	31.88	32.30	36.33	33.43	32.89
GOF		107.54	91.09	76.37	63.68	58.24	173.26	95.03
2DGS		68.47	62.24	65.02	63.14	62.32	77.46	66.44
Ours		205.55	178.29	209.90	170.30	148.75	298.66	201.91

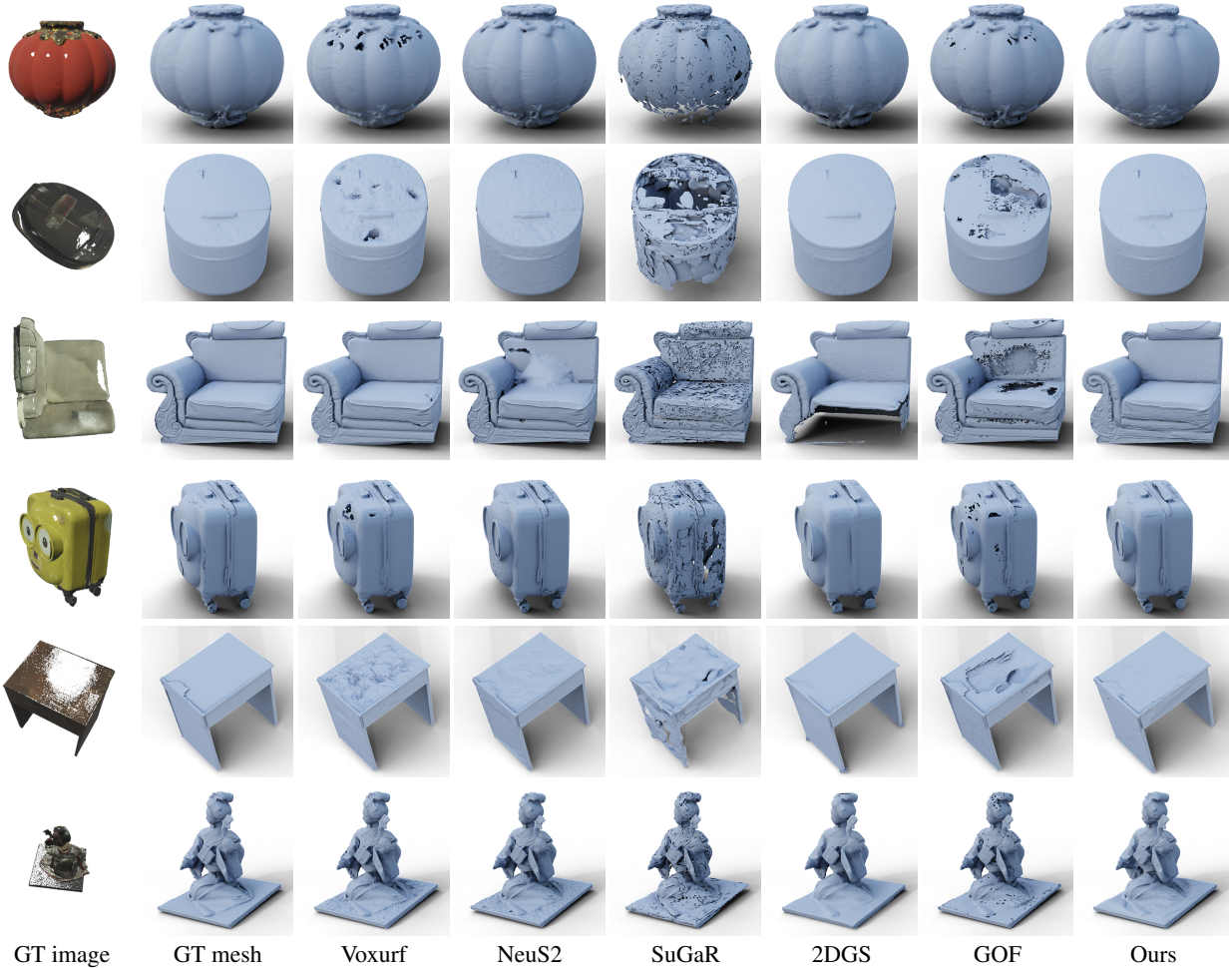


Figure 8: Visual comparison of geometric reconstruction results on the OO3D-SL dataset.

5 Experiments

5.1 Setup

Implementation. We realize our method before stage 4 by creating a specialized PyTorch CUDA extension library, which greatly improves the speed of reconstruction. We conducted our experiments on an NVIDIA A100 GPU with 40 GB memory and the octree construction can be completed in an hour. For the 3D Gaussian optimization, we optimize the model by 30k iterations in about 15 minutes.

Dataset. We conducted the experiments on two datasets, the OmniObject3D Wu et al. [2023b] dataset and the NeRF-Synthetic dataset. We selected 24 real objects (6 categories, each with 4 objects) that are affected by strong light and result in large areas of specular highlights on the surface, and we named it OO3D-SL dataset. For each object, there are 90 training images and 10 test images. Moreover, we also compare the results on the NeRF-Synthetic dataset Mildenhall et al. [2021]. This dataset contains a total of 8 objects. Each scene contains 100 images for training with a resolution of 800×800 generated from different angles and 200 test images. For the evaluation metrics, we evaluated the Peak-to-Noise Ratio (PSNR), Frames Per Second (FPS) and Chamfer Distance (CD in 10^{-4}). For some reconstructed models, due to occlusion or self-occlusion, there are parts of the 3D objects that remain unseen in any of the input images, such as the base of a rice cooker. We remove these parts before computing CD to measure geometric quality. In our experiments, we selected Voxurf Wu et al. [2023a], NeuS2 Wang et al. [2023a], 3DGS Kerbl et al. [2023], SuGaR Guédon and Lepetit [2024], GOF Yu et al. [2024] and 2DGS Huang et al. [2024] as the baseline methods for comparison.

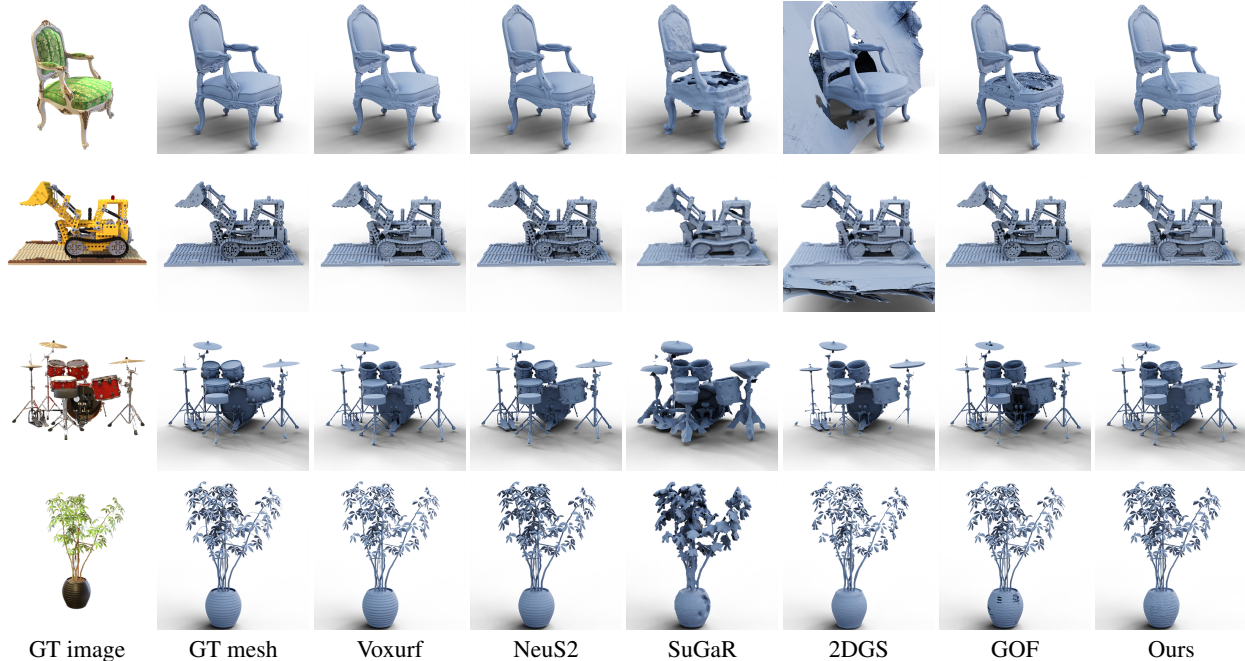


Figure 9: Visual comparison of geometric reconstruction results on the NeRF-Synthetic dataset.

5.2 Results

As shown in Tab. 1 and Fig. 8, the surface reconstructed by SuGaR Guédon and Lepetit [2024] is discontinuous with holes, which is not good at reconstructing objects. Voxurf Wu et al. [2023a] and GOF Yu et al. [2024] are sensitive to strong light and there are many holes in the surface. The quality of the geometric reconstruction from NeuS2 Wang et al. [2023a] is close to ours, however, there are still a small number of objects affected by the strong light causing holes and wrong surface. 2DGS Huang et al. [2024] is almost unaffected by strong light, however, the object surface lacks detail and is poor for reconstruction of areas with fewer viewing directions. Moreover, it sometimes reconstructs the background that is not present in the images, and these redundancies are connected to the object which cannot be easily removed (see the examples of Chair and Lego in Fig. 9). Of all the comparison methods, our method obtains the highest geometric quality in the OO3D-SL dataset, and the reconstructed geometry is also comparable to these state-of-the-art methods in the non-strong light dataset such as NeRF-Synthetic (see Fig. 9). More visualization results of geometry can be seen in the appendix.

When it comes to novel view synthesis results, our methods also shows competitive quality compared with recent methods. We analyse the synthesis quality with PSNR and rendering FPS. As shown in Tab. 1 and Fig. 10, our results achieve PSNR comparable to the SDF-based methods, such as Voxurf Wu et al. [2023a] and NeuS2 Wang et al. [2023a]. Due to the incompleteness of reconstructed meshes, SuGaR Guédon and Lepetit [2024] performs slightly worse than other 3DGS-based methods, such as 2DGS Huang et al. [2024] and GOF Yu et al. [2024]. Although our PSNR performance is slightly lower than theirs, we keep the efficient rendering speed inherited from 3DGS Kerbl et al. [2023]. Only our method reaches comparable FPS to 3DGS, as shown in Tab. 1. Other 3DGS-based methods Guédon and Lepetit [2024], Huang et al. [2024], Yu et al. [2024] either have more computational costs or use their own rendering pipeline, and that reduces their rendering speed. For the non-3DGS-based methods Wu et al. [2023a], Wang et al. [2023a], their rendering speed is slow because of the volume rendering pipeline from NeRF Mildenhall et al. [2021] and extra network inference time. Moreover, for all 3DGS-based methods Kerbl et al. [2023], Guédon and Lepetit [2024], Huang et al. [2024], Yu et al. [2024], we also report the number of 3D Gaussians in thousands, N_{GS} , as shown in Fig. 10. Our method uses a much smaller number of 3D Gaussians for most objects, especially in the OO3D-SL dataset, by effectively pruning redundant 3D Gaussians with our SDF supervision.

We present our qualitative comparison result of different methods in Tab. 2. Our method is mainly developed for object-level targets. These methods Guédon and Lepetit [2024], Huang et al. [2024], Yu et al. [2024] can reconstruct satisfying geometries for scene-level targets, but they are not good at object-level reconstruction. Meanwhile, our method successfully reconstructs the object under strong lighting and preserves the details of the object. For rendering quality, our method slightly falls back to the recent 3DGS-based method but is still competitive with non-3DGS-based



Figure 10: Visual comparison of image rendering results on the OO3D-SL dataset and the NeRF-synthetic dataset. Our method achieves high rendering speed while maintaining comparable image rendering quality to other methods. Moreover, our method reduces the number of redundant Gaussians, making the model more compact. The 3-tuple below each figure represents the PSNR, FPS and the number of Gaussians (in thousands), with the best results highlighted in bold.

methods. Finally, only our method keeps a similar rendering speed to 3DGS Kerbl et al. [2023], thanks to the efficient rasterization module from 3DGS. Other methods either have extra computational costs from the MLP network or use different rendering pipelines, thus being unable to efficiently render images. Also, our method is capable of real-time rendering (60+ FPS) with a much higher resolution, e.g., 2048×2048 .

5.3 Ablation Studies

We conduct ablation studies on the opacity loss and the scale loss mentioned in Sec. 4.3. We evaluate the performance of the baseline 3DGS Kerbl et al. [2023] and our method, with opacity loss and scale loss activated or not. We conduct the experiment on OO3D-SL Wu et al. [2023b] dataset and report PSNR and number of 3D Gaussians N_{GS} . As shown

Table 2: Qualitative comparison of different methods.

	Main Target	Geometry Quality	Rendering Quality	Rendering Speed
Voxurf Wu et al. [2023a]	Object	Middle	High	Low
NeuS2 Wang et al. [2023a]	Object	High	High	Low
3DGS Kerbl et al. [2023]	Scene	Low	High	High
SuGaR Guédon and Lepetit [2024]	Scene	Middle	Middle	Middle
2DGS Huang et al. [2024]	Scene	Middle	High	Middle
GOF Yu et al. [2024]	Scene	Middle	High	Middle
Ours	Object	High	Middle	High

Table 3: Ablation on the loss terms.

Method	PSNR	N_{GS}
3DGS	36.28	+0.00%
w/ \mathcal{L}_{scale} & w/o \mathcal{L}_{op}	36.28	+0.79%
w/ \mathcal{L}_{op} & w/o \mathcal{L}_{scale}	35.15	-50.17%
w/ \mathcal{L}_{op} & w/ \mathcal{L}_{scale} (Ours)	35.18	-52.33%

in Tab. 3, the opacity loss is an essential condition for 3D Gaussian pruning. It significantly reduces N_{GS} , by more than 50%. The scale loss does not contribute when locations of 3D Gaussians are not near the surface. In other words, it only works when opacity loss is activated and the 3D Gaussians are pulled towards the surface.

6 Conclusion

In this study, we optimize an octree-based Gaussian splatting representation for reconstructing object-level implicit surface and radiation fields under strong lighting. The method confirms the possibility that Gaussians can guide geometric optimization, and good geometry can further optimize Gaussian points. Our method is robust to strong lighting and can reconstruct detailed object-level geometries, while retaining the advantages of real-time high-quality rendering of Gaussian splatting.

References

- Ben Mildenhall, Pratul P Srinivasan, Matthew Tancik, Jonathan T Barron, Ravi Ramamoorthi, and Ren Ng. Nerf: Representing scenes as neural radiance fields for view synthesis. *Communications of the ACM*, 65(1):99–106, 2021.
- Jonathan T Barron, Ben Mildenhall, Matthew Tancik, Peter Hedman, Ricardo Martin-Brualla, and Pratul P Srinivasan. Mip-nerf: A multiscale representation for anti-aliasing neural radiance fields. In *Proceedings of the IEEE/CVF International Conference on Computer Vision*, pages 5855–5864, 2021.
- Jonathan T Barron, Ben Mildenhall, Dor Verbin, Pratul P Srinivasan, and Peter Hedman. Mip-nerf 360: Unbounded anti-aliased neural radiance fields. In *Proceedings of the IEEE/CVF Conference on Computer Vision and Pattern Recognition*, pages 5470–5479, 2022.
- Sara Fridovich-Keil, Alex Yu, Matthew Tancik, Qinhong Chen, Benjamin Recht, and Angjoo Kanazawa. Plenoxels: Radiance fields without neural networks. In *Proceedings of the IEEE/CVF Conference on Computer Vision and Pattern Recognition*, pages 5501–5510, 2022.
- Tong Wu, Jiaqi Wang, Xingang Pan, Xudong Xu, Christian Theobalt, Ziwei Liu, and Dahua Lin. Voxurf: Voxel-based efficient and accurate neural surface reconstruction. In *International Conference on Learning Representations (ICLR)*, 2023a.
- Cheng Sun, Min Sun, and Hwann-Tzong Chen. Direct voxel grid optimization: Super-fast convergence for radiance fields reconstruction. In *Proceedings of the IEEE/CVF Conference on Computer Vision and Pattern Recognition*, pages 5459–5469, 2022a.
- Lingjie Liu, Jiatao Gu, Kyaw Zaw Lin, Tat-Seng Chua, and Christian Theobalt. Neural sparse voxel fields. *Advances in Neural Information Processing Systems*, 33:15651–15663, 2020.
- Cheng Sun, Min Sun, and Hwann-Tzong Chen. Improved direct voxel grid optimization for radiance fields reconstruction. *arXiv preprint arXiv:2206.05085*, 2022b.
- Bernhard Kerbl, Georgios Kopanas, Thomas Leimkühler, and George Drettakis. 3d gaussian splatting for real-time radiance field rendering. *ACM Transactions on Graphics*, 42(4), July 2023.
- Antoine Guédon and Vincent Lepetit. Sugar: Surface-aligned gaussian splatting for efficient 3d mesh reconstruction and high-quality mesh rendering. *CVPR*, 2024.
- Hanlin Chen, Chen Li, and Gim Hee Lee. Neusg: Neural implicit surface reconstruction with 3d gaussian splatting guidance. *arXiv preprint arXiv:2312.00846*, 2023.
- Jiaxiang Tang, Jiawei Ren, Hang Zhou, Ziwei Liu, and Gang Zeng. Dreamgaussian: Generative gaussian splatting for efficient 3d content creation. 2024.

- Taoran Yi, Jiemin Fang, Junjie Wang, Guanjun Wu, Lingxi Xie, Xiaopeng Zhang, Wenyu Liu, Qi Tian, and Xinggang Wang. Gaussiandreamer: Fast generation from text to 3d gaussians by bridging 2d and 3d diffusion models. In *CVPR*, 2024.
- Zehao Yu, Torsten Sattler, and Andreas Geiger. Gaussian opacity fields: Efficient and compact surface reconstruction in unbounded scenes. *arXiv preprint arXiv:2404.10772*, 2024.
- Binbin Huang, Zehao Yu, Anpei Chen, Andreas Geiger, and Shenghua Gao. 2d gaussian splatting for geometrically accurate radiance fields. In *SIGGRAPH 2024 Conference Papers*. Association for Computing Machinery, 2024. doi:10.1145/3641519.3657428.
- Yiming Wang, Qin Han, Marc Habermann, Kostas Daniilidis, Christian Theobalt, and Lingjie Liu. Neus2: Fast learning of neural implicit surfaces for multi-view reconstruction. In *Proceedings of the IEEE/CVF International Conference on Computer Vision (ICCV)*, 2023a.
- Lior Yariv, Jiatao Gu, Yoni Kasten, and Yaron Lipman. Volume rendering of neural implicit surfaces. In *NeurIPS'21*, pages 4805–4815, 2021.
- Peng Wang, Lingjie Liu, Yuan Liu, Christian Theobalt, Taku Komura, and Wenping Wang. Neus: Learning neural implicit surfaces by volume rendering for multi-view reconstruction. *NeurIPS*, 2021.
- Lior Yariv, Yoni Kasten, Dror Moran, Meirav Galun, Matan Atzmon, Ronen Basri, and Yaron Lipman. Multiview neural surface reconstruction by disentangling geometry and appearance. In *Proceedings of the 34th International Conference on Neural Information Processing Systems*, 2020.
- Michael Niemeyer, Lars Mescheder, Michael Oechsle, and Andreas Geiger. Differentiable volumetric rendering: Learning implicit 3d representations without 3d supervision. In *Proceedings of the IEEE/CVF Conference on Computer Vision and Pattern Recognition*, pages 3504–3515, 2020.
- Thomas Müller, Alex Evans, Christoph Schied, and Alexander Keller. Instant neural graphics primitives with a multiresolution hash encoding. *ACM Transactions on Graphics (ToG)*, 41(4):1–15, 2022.
- Radu Alexandru Rosu and Sven Behnke. Permutosdf: Fast multi-view reconstruction with implicit surfaces using permutohedral lattices. In *Proceedings of the IEEE/CVF Conference on Computer Vision and Pattern Recognition*, pages 8466–8475, 2023.
- Zhaoshuo Li, Thomas Muller, Alex Evans, Russell H. Taylor, M. Unberath, Ming-Yu Liu, and Chen-Hsuan Lin. Neuralangelo: High-fidelity neural surface reconstruction. *2023 IEEE/CVF Conference on Computer Vision and Pattern Recognition (CVPR)*, pages 8456–8465, 2023.
- Anpei Chen, Zexiang Xu, Andreas Geiger, Jingyi Yu, and Hao Su. Tensorf: Tensorial radiance fields. In *European Conference on Computer Vision*, pages 333–350. Springer, 2022.
- Quankai Gao, Qiangeng Xu, Hao Su, Ulrich Neumann, and Zexiang Xu. Strivec: Sparse tri-vector radiance fields. In *Proceedings of the IEEE/CVF International Conference on Computer Vision (ICCV)*, 2023.
- Stephan J Garbin, Marek Kowalski, Matthew Johnson, Jamie Shotton, and Julien Valentin. Fastnerf: High-fidelity neural rendering at 200fps. In *Proceedings of the IEEE/CVF International Conference on Computer Vision*, pages 14346–14355, 2021.
- Alex Yu, Ruilong Li, Matthew Tancik, Hao Li, Ren Ng, and Angjoo Kanazawa. Plenotrees for real-time rendering of neural radiance fields. In *Proceedings of the IEEE/CVF International Conference on Computer Vision*, pages 5752–5761, 2021.
- Liao Wang, Jiakai Zhang, Xinhang Liu, Fuqiang Zhao, Yanshun Zhang, Yingliang Zhang, Minye Wu, Jingyi Yu, and Lan Xu. Fourier plenotrees for dynamic radiance field rendering in real-time. In *Proceedings of the IEEE/CVF Conference on Computer Vision and Pattern Recognition*, pages 13524–13534, 2022.
- Zixi Shu, Ran Yi, Yuqi Meng, Yutong Wu, and Lizhuang Ma. Rt-octree: Accelerate plenotree rendering with batched regular tracking and neural denoising for real-time neural radiance fields. In *SIGGRAPH Asia 2023 Conference Papers*, pages 1–11, 2023.
- Lior Yariv, Peter Hedman, Christian Reiser, Dor Verbin, Pratul P. Srinivasan, Richard Szeliski, Jonathan T. Barron, and Ben Mildenhall. Baked sdf: Meshing neural sdfs for real-time view synthesis. In *ACM SIGGRAPH 2023 Conference Proceedings*, 2023.
- Tao Lu, Mulin Yu, Linning Xu, Yuanbo Xiangli, Limin Wang, Dahua Lin, and Bo Dai. Scaffold-gs: Structured 3d gaussians for view-adaptive rendering. *CVPR*, 2024.
- Butian Xiong, Zhuo Li, and Zhen Li. Gauu-scene: A scene reconstruction benchmark on large scale 3d reconstruction dataset using gaussian splatting. *arXiv preprint arXiv:2401.14032*, 2024.

Xiaoyang Lyu, Yang-Tian Sun, Yi-Hua Huang, Xiuzhe Wu, Ziyi Yang, Yilun Chen, Jiangmiao Pang, and Xiaojuan Qi. 3dgsr: Implicit surface reconstruction with 3d gaussian splatting. *arXiv preprint arXiv:2404.00409*, 2024.

Ben Fei, Jingyi Xu, Rui Zhang, Qingyuan Zhou, Weidong Yang, and Ying He. 3d gaussian splatting as new era: A survey. *IEEE Transactions on Visualization and Computer Graphics*, pages 1–20, 2024.

Tong Wu, Yu-Jie Yuan, Ling-Xiao Zhang, Jie Yang, Yan-Pei Cao, Ling-Qi Yan, and Lin Gao. Recent advances in 3d gaussian splatting. *CoRR*, abs/2403.11134, 2024.

Guikun Chen and Wenguan Wang. A survey on 3d gaussian splatting. *CoRR*, abs/2401.03890, 2024.

Jane Wilhelms and Allen Van Gelder. Octrees for faster isosurface generation. *ACM Transactions on Graphics (TOG)*, 11(3):201–227, 1992.

William E Lorensen and Harvey E Cline. Marching cubes: A high resolution 3d surface construction algorithm. In *Seminal graphics: pioneering efforts that shaped the field*, pages 347–353. 1998.

Albert Pumarola, Artsiom Sanakoyeu, Lior Yariv, Ali Thabet, and Yaron Lipman. Visco grids: Surface reconstruction with viscosity and coarea grids. In S. Koyejo, S. Mohamed, A. Agarwal, D. Belgrave, K. Cho, and A. Oh, editors, *Advances in Neural Information Processing Systems*, volume 35, pages 18060–18071. Curran Associates, Inc., 2022.

Zixiong Wang, Yunxiao Zhang, Rui Xu, Fan Zhang, Peng Wang, Shuangmin Chen, Shiqing Xin, Wenping Wang, and Changhe Tu. Neural-singular-hessian: Implicit neural representation of unoriented point clouds by enforcing singular hessian. *ACM Transactions on Graphics*, 42:1 – 14, 2023b.

Tong Wu, Jiarui Zhang, Xiao Fu, Yuxin Wang, Jiawei Ren, Liang Pan, Wayne Wu, Lei Yang, Jiaqi Wang, Chen Qian, Dahua Lin, and Ziwei Liu. Omniobject3d: Large-vocabulary 3d object dataset for realistic perception, reconstruction and generation. *IEEE/CVF Conference on Computer Vision and Pattern Recognition (CVPR)*, 2023b.

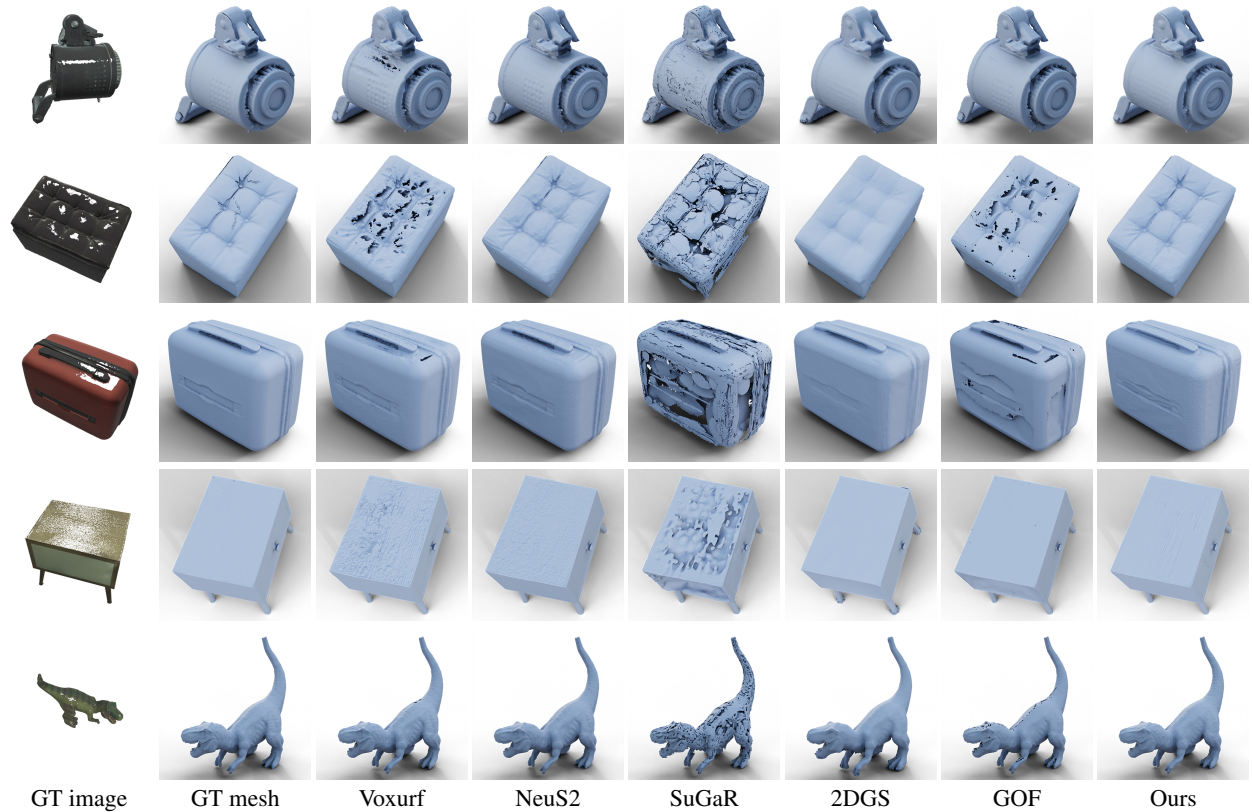
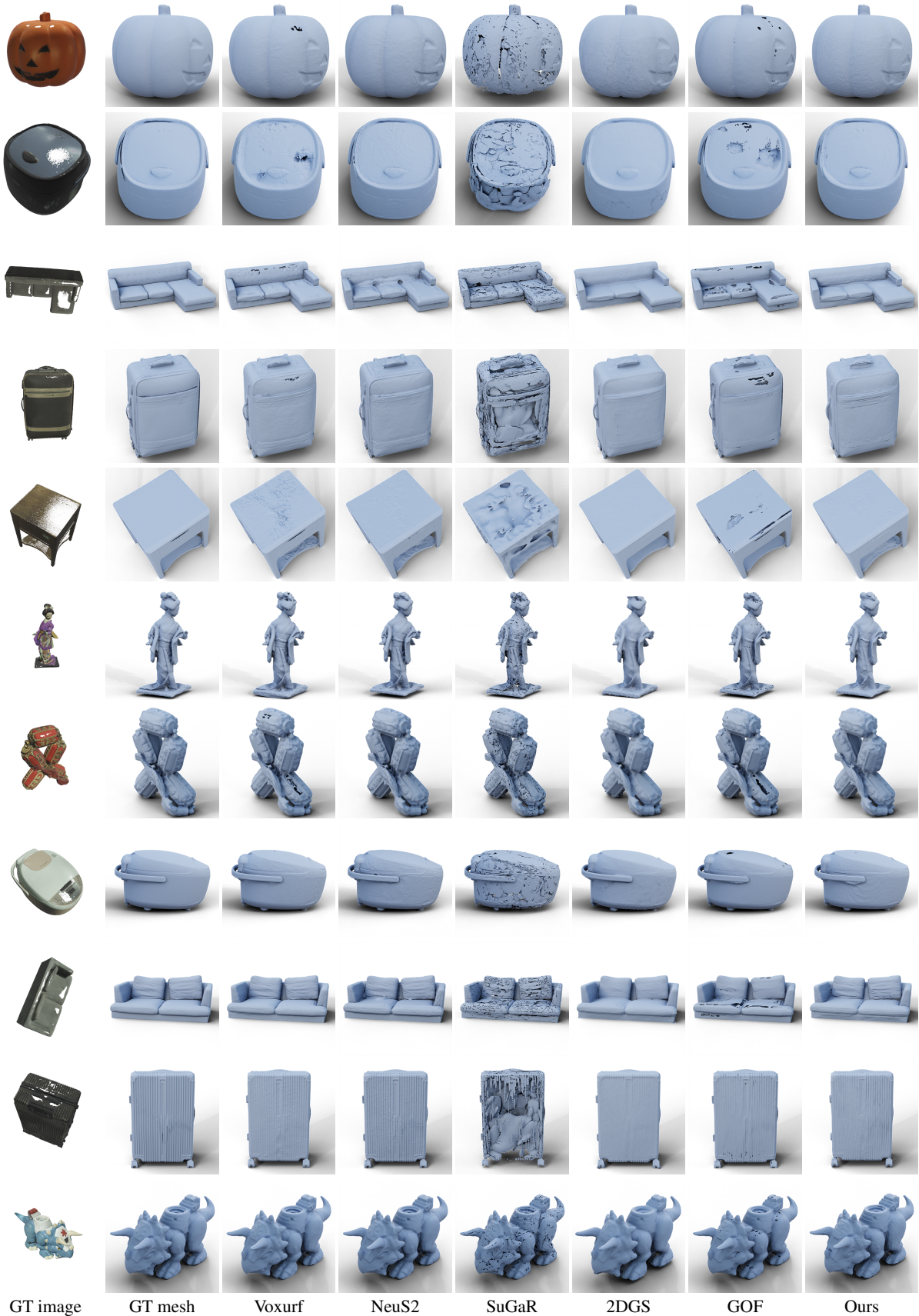


Figure 11: More comparison of geometric reconstruction results on the OO3D-SL dataset.



GT image

GT mesh

Voxurf

NeuS2

SuGaR

2DGS

GOF

Ours

Figure 12: More comparison of geometric reconstruction results on the OO3D-SL dataset.

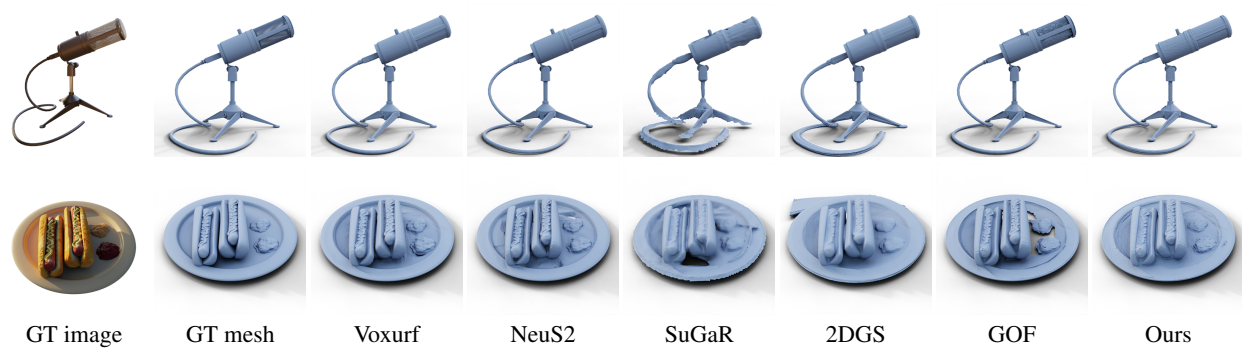


Figure 13: More comparison of geometric reconstruction results on the NeRF-Synthetic dataset.